

Impedance boundary conditions for general transient hemodynamics

Will Cousins^{1,*},† and Pierre A. Gremaud²

¹*Department of Mechanical Engineering, Massachusetts Institute of Technology, Boston, MA 02139, USA*

²*Department of Mathematics, North Carolina State University, Raleigh, NC 27695, USA*

SUMMARY

We discuss the implementation and calibration of a new generalized structured tree boundary condition for hemodynamics. The main idea is to approximate the impedance corresponding to the vessels downstream from a specific outlet. Unlike previous impedance conditions, the one considered here is applicable to general transient flows as opposed to periodic ones only. The physiological character of the approach significantly simplifies calibration. We also describe a novel way to incorporate autoregulation mechanisms in structured arterial trees at minimal computational cost. The strength of the approach is illustrated and validated on several examples through comparison with clinical data. Copyright © 2014 John Wiley & Sons, Ltd.

Received 24 August 2013; Revised 25 March 2014; Accepted 23 April 2014

KEY WORDS: hemodynamics; boundary conditions; autoregulation; impedance; vascular trees

1. INTRODUCTION

A common goal of computational hemodynamics studies is the numerical prediction of blood flow downstream from stem arteries in which measurements are available. For instance, one might be interested in blood perfusion in the middle cerebral artery (MCA) territory given measured values of the blood velocity in the MCA itself. Because of computational complexity and uncertainties about the geometry of the vasculature, such calculations are usually only performed in a small number of contiguous vessels. At the downstream edge of the computational domain, outflow boundary conditions are imposed. Ideally, these conditions

1. model faithfully the influence of the vasculature that is not included in the computational domain,
2. lead to a mathematically well defined and numerically tractable set of equations,
3. contain parameters that can either be directly measured or easily calibrated, and
4. are straightforward to implement and computationally inexpensive.

We propose an approach that, in addition, can be applied to general transient flows and requires calibration of only a few parameters because of its inherent physiological nature.

It is possible to derive outflow boundary conditions for a fluid flowing in a vessel by relating the pressure drop P along the vessel (or network of vessels) to the flux Q through that vessel (or set of vessels). In the simplest case of an established flow, that is, no time dependence, P and Q are linearly related through $P = R Q$ where R is a resistance value; this is Darcy's law. This relation has been used in hemodynamics [1–3] by assuming the frequency of the flow (roughly 1 Hz) to be low enough for the instantaneous value of Q at time t , $Q(t)$, to depend only on the instantaneous

*Correspondence to: Will Cousins, Department of Mechanical Engineering, Massachusetts Institute of Technology, Boston, MA 02139, USA.

†E-mail: wcousins@mit.edu

value of P at that time, $P(t)$. This purely resistive condition has several drawbacks; in particular, it may lead to unrealistic values and also forces the flow rate and pressure to be in phase [4–6].

For general transient flows, there is no reason for a direct relation between $P(t)$ and $Q(t)$ to exist. In [7–9], Olufsen worked instead with each spectral component of P and Q , obtained through Fourier analysis, and defined a frequency dependent complex version of R , that is, an impedance. This approach is based on the assumption that, downstream of an outflow vessel, the vessels form a fractal (finite) tree. It is also limited to periodic flows. In [10], we retained the geometric assumptions of [7–9] but defined the impedance of a vascular tree through its Laplace—instead of Fourier—transform, see (2) in the succeeding text. This allows for the simulation of general transient flows.

In this study, we begin by briefly summarizing our generalized structured tree boundary condition, which was originally developed in [10] (Sections 2.1 and 2.2). In Section 2.3, we discuss new adjustments to the structured tree; although minor, they lead to significant improvements. As noted in [11], users are often required to use physically unrealistic values for the tree's governing parameters in order to obtain accurate simulation results. The physiologically based modifications of Section 2.3 correct this: we obtain results agreeing well with *in vivo* data using realistic tree parameters in Section 3.1.

We incorporate autoregulation into the tree formulation in Section 2.5 by including vasodilation and vasoconstriction of the smaller arteries. This approach requires minimal computational cost. Our approach is compatible with a broad class of autoregulation models. Our results in Section 3.3 agree well with clinical data for three considered experiments.

2. METHOD

The derivation of the generalized structured tree condition [10] relies on three steps. First, the impedance at the beginning of a vessel (inflow) is expressed as a function of the impedance at the end of that vessel (outflow) (Section 2.1). Second, through continuity and conservation principles, impedance values are recursively propagated through the entire tree (Section 2.2). Third, the obtained impedance is turned into an implementable outflow boundary condition (Section 2.4).

2.1. Impedance of a single vessel

The approach is based on the linearization and cross-sectional averaging of the incompressible Navier-Stokes equations in elastic axisymmetric cylindrical vessels [11–15]. The system is closed with a constitutive relation linking the pressure P to the cross-sectional area A

$$P = \mathcal{P}(A) \Leftrightarrow A = \mathcal{A}(P).$$

In this work, we use the following relation from Olufsen [8]:

$$P - P_0 = \frac{4Eh}{3r_0} \left(1 - \sqrt{\frac{A_0}{A}} \right), \quad (1)$$

where $A_0 = \pi r_0^2$ is the unstressed cross-sectional area of the vessel, r_0 being the unstressed vessel radius, and E and h are the Young modulus and thickness of the vessel wall, respectively.

The resulting equations can be solved analytically by expressing the unknowns in terms of their Fourier coefficients [7–9, 11, 16]. To treat general transient flows, we take instead the Laplace transform of the system with respect to time and define the impedance Z through its Laplace transform $\hat{Z} = \mathcal{L}(Z)$ by

$$\hat{Z}(x, s) = \frac{\hat{P}(x, s)}{\hat{Q}(x, s)}, \quad (2)$$

where x measures the longitudinal distance along the vessel and s is a generic complex number; \hat{P} and \hat{Q} are the Laplace transforms of the pressure P and the flow rate Q . For a vessel of length L , the impedance satisfies [10]

$$\hat{Z}(0, s) = \frac{\hat{Z}(L, s) + \frac{1}{sd_s C} \tanh L/d_s}{sd_s C \hat{Z}(L, s) \tanh L/d_s + 1}, \quad (3)$$

where $C = dA/dP|_{P=p_0}$ is the vessel compliance. In addition, $d_s^2 = A_0/[C\rho s(s + \delta)]$ and $\delta = 2\mu(\gamma + 2)/(\rho r_0^2)$ where μ and ρ are the blood viscosity and density. In the previous derivation, the parameter γ defines the radial profile of the longitudinal velocity; $\gamma = 2$ corresponds to the classical Poiseuille flow.

A strength of the structured tree approach is that a user is not necessarily required to use our particular model. If one prefers an alternative hemodynamic model or constitutive model for the arterial wall, it would be straightforward to derive an analogous version of the impedance relation (3) using these alternative models through simple linearization.

2.2. Impedance of a vascular tree

We consider vascular trees with the following structure [7–11] and constant scaling parameters throughout:

1. All vessels have the same aspect ratio $\lambda = L/r$.
2. Each vessel bifurcates into two daughter vessels unless its radius is less than a minimum radius $r_{min} > 0$, in which case it terminates.
3. The relationship between the parent vessel radius r_p and the daughter vessels' radii r_{d1} and r_{d2} is characterized by two constant scaling factors α and β such that

$$r_{d1} = \alpha r_p \text{ and } r_{d2} = \beta r_p.$$

A vascular tree is thus determined by the four parameters α , β , λ , and r_{min} along with the radius of the root vessel r_{root} .

At junctions, we assume continuity of the pressure and conservation of mass, which yields by (2)

$$\frac{1}{\hat{Z}_p(L, s)} = \frac{1}{\hat{Z}_{d1}(0, s)} + \frac{1}{\hat{Z}_{d2}(0, s)}, \quad (4)$$

for any complex number s . The impedance at the end of terminal vessels is set to a common value \hat{Z}_{term} , and the impedance of a root vessel is found by applying recursively relations (3) and (4), see Sections 2.3 and 2.4.

2.3. Parameter choices

We consider three additional modifications to the structured tree boundary condition.

First, the choice of the minimum radius r_{min} (radius of terminal vessels) is delicate because there are in fact no terminal vessels at the bottom of the tree but rather a transition to the venous side of the vasculature. Further, the tree impedances depend strongly and non-smoothly on r_{min} [11, 17]. In the context of structured tree boundary conditions, values ranging from $3 \mu\text{m}$ to $600 \mu\text{m}$ have been used [8, 9, 11, 16–19]. At the capillary level, the vascular network no longer resembles a fractal tree but is more accurately described by a complex, mesh like structure [20]. Thus, we choose $r_{min} = 30 \mu\text{m}$ because our binary tree description is likely inaccurate for capillary vessels of radii smaller than this value.

Second, while the choice $\hat{Z}_{term} = 0$ is standard [8–11, 17, 18], elementary arguments show this value to be drastically unrealistic [17]. One possible way to rectify this issue would be to determine physiologically appropriate values of \hat{Z}_{term} to impose at the terminal vessels. However, doing so would require somewhat detailed knowledge of the relationship between pressure and

flow rate at these terminal vessels. A simpler solution is to impose a constant terminal pressure, P_{term} . Including this terminal pressure modifies (2) so that the corresponding time domain expression becomes

$$P(t) = \int_0^t Z(\tau)Q(t - \tau) d\tau + P_{term}, \tag{5}$$

where $\mathcal{L}[Z] = \hat{Z}$, where \hat{Z} is the impedance at the root of the tree computed with $\hat{Z}_{term} = 0$ (see [17] for discussion and further justification). Pressure values of roughly 45 mmHg have been reported at the level at which we terminate the tree ($r_{min} = 30 \mu m$) [7, 21]. We use $P_{term} = 45$ mmHg in all simulations here.

Third, we consider the radius dependent relative effective viscosity proposed in [22] (relations (9) and (10)) for a normal hematocrit value of 0.45

$$\mu_{rel} = \left[1 + (\mu^* - 1) \left(\frac{D}{D - 1.1} \right)^2 \right] \left(\frac{D}{D - 1.1} \right)^2,$$

$$\mu^* = 6 e^{-0.085D} + 3.2 - 2.44 e^{-0.06D^{0.645}},$$

where D is the diameter of the vessel measured in microns (μm). We use $\mu = 0.0488 \mu_{rel}/3.2$ in (3) to ensure that $\mu \approx 0.0488 \text{ g} \times \text{cm}^{-1} \times \text{s}^{-1}$ when D is large, where the viscosity shows little dependence on vessel diameter [22, 23]. Finally, we take $\alpha = 0.91, \beta = 0.58$. These values were proposed in [8] after an investigation of measured and theoretically optimal values. These and other parameters used in the proposed boundary condition are summarized in Table I.

2.4. Implementation

The direct implementation of (5) would require the calculation of the inverse Laplace transform of \hat{Z} , an ill-conditioned numerical operation [24]. We take instead a convolution quadrature approach,

Table I. Parameters and their values involved in the proposed boundary condition.

	Parameter	Value/expression
Fluid	μ : blood viscosity	See Section 2.3
	ρ : blood density	1.06 g cm ⁻³
	γ : velocity profile	2
	P_{term} : terminal pressure	45 mmHg
	\hat{Z}_{term} : terminal impedance	0
Elasticity [8]	C : compliance	$\frac{3}{2} \pi r_0^2 \frac{r_0}{Eh}$
	$\frac{Eh}{r}$	$k_1 e^{k_2 r} + k_3$
	k_1	$2.00 \times 10^7 \text{ gs}^{-2} \text{cm}^{-1}$
	k_2	-22.53 cm^{-1}
	k_3	$8.65 \times 10^5 \text{ gs}^{-2} \text{cm}^{-1}$
Geometry	α : radii ratio	0.91
	β : radii ratio	0.58
	λ : length/radius ratio	Variable
	r_{root} : root/outflow vessel radius	Variable
	r_{min} : minimum radius	30 μm
Autoregulation	G_{AR} : autoregulation gain	4
Numerics	t_f : final simulation time	Variable
	Δt : time step	Variable
	N : number of time steps	$t_f / \Delta t$
	ϵ : accuracy parameter	10^{-10}

which only requires the value of \hat{Z} rather than Z [25, 26]. This results in the following boundary condition to be enforced at the end of the outflow vessel:

$$P_n = \sum_{k=0}^n z_k Q_{n-k} + P_{term}. \quad (6)$$

In (6), P_n is the value of the pressure at the n -th time step, and Q_k is the value of the flow rate at the k -th time step, assuming a constant time step Δt .

We now describe how to compute the impedance weights z_k , $k = 0, \dots, N$. Although N should formally be taken as the total number of time steps, this choice could be computationally costly for long time simulations. Choosing $N = \text{ceil}(1/\Delta t)$ (smallest following integer to $1/\Delta t$) gives nearly identical results without any accuracy loss because the values of z_k converge quickly to 0 as k becomes large [10, 17]. An example of this convergence behavior is displayed in Figure 1, left. This convergence behavior was observed universally in all trees considered in this work. Furthermore, z_k can be viewed as a measure of the relationship between the pressure at time t and the flow rate at time $t - k\Delta t$. One would not expect strong relationships between the pressure at a particular time and the flow rate in the distant past, which suggests that z_k should converge to 0 as $k \rightarrow \infty$.

The algorithm essentially consists of the three functions described in the succeeding text. The function `SINGLEVESSELIMP` merely implements (3). The `IMPEDANCE` function corresponds to the iterative process described at the end of Section 2.2, where (3) and (4) are recursively applied to compute the impedance $\hat{Z}(s)$ at the root of the structured tree. The `IMPEDANCEWEIGHTS` function computes the impedance weights z_k entering (6). The function `IMPEDANCEWEIGHTS` performs the convolution quadrature approach developed by Lubich [25, 26]. For additional insight into the meaning of the steps performed in `IMPEDANCEWEIGHTS`, please refer to [25] or [10]. Additional justification and explanation for all algorithms are available in [10].

function `IMPEDANCEWEIGHTS`(r_{root} , Δt , ϵ)

Inputs: r_{root} - radius of the outlet vessel

Δt - time step size

ϵ - numerical accuracy of `IMPEDANCE` function (we use 10^{-10})

Output: impedance weights z_n , $n = 0, \dots, N$

$N = \text{ceil}(1/\Delta t)$

$\eta = \epsilon^{1/2N}$

for $m = 0 : 2N - 1$ **do**

$\zeta = \eta e^{i\pi m/N}$

$\mathcal{E} = \frac{1}{2}\zeta^2 - 2\zeta + \frac{3}{2}$

table = array of NaN

$Z^{(m)} = \text{IMPEDANCE}(r_{root}, \mathcal{E}/\Delta t, 1, 1, \text{table})$

end for

for $n = 0 : N$ **do**

$z_n = \frac{\eta^{-n}}{2N} \sum_{m=0}^{2N-1} Z^{(m)} e^{-i\pi mn/N}$

end for

end function

2.5. Incorporation of autoregulatory mechanisms

Cerebral autoregulation refers to the adaptive dilation or contraction of vessels (primarily the smaller arteries) to maintain a relatively constant flow rate despite changes in pressure [27–29]. Vasodilation/constriction can be induced by a variety of mechanisms including myogenic [30], neurogenic [31, 32], shear stress-based [33], and metabolic mechanisms [34, 35]. Situations involving strong autoregulatory effects are prime examples of non-periodic flow conditions. While previous versions of the structured tree boundary condition are restricted to periodic flows, our generalized

```

function IMPEDANCE( $s, r_{root}, N_{\alpha}, N_{\beta}, \text{table}$ ) ▷ recursive function
Output: Laplace transform of tree impedance

 $r_0 = r_{root} \alpha^{N_{\alpha}-1} \beta^{N_{\beta}-1}$ 
if  $r_0 < r_{min}$  then
     $ZL = Z_{term}$ 
else
    if  $\text{table}(N_{\alpha} + 1, N_{\beta})$  is NaN then
         $[ZD1, \text{table}] = \text{IMPEDANCE}(s, r_{root}, N_{\alpha} + 1, N_{\beta}, \text{table})$ 
    else
         $ZD1 = \text{table}(N_{\alpha} + 1, N_{\beta})$ 
    end if

    if  $\text{table}(N_{\alpha}, N_{\beta} + 1)$  is NaN then
         $[ZD2, \text{table}] = \text{IMPEDANCE}(s, r_{root}, N_{\alpha}, N_{\beta} + 1, \text{table})$ 
    else
         $ZD2 = \text{table}(N_{\alpha}, N_{\beta} + 1)$ 
    end if
     $ZL = ZD1 \cdot ZD2 / (ZD1 + ZD2)$ 
end if

 $Z0 = \text{SINGLEVESSELIMP}(ZL, s)$ 
 $\text{table}(N_{\alpha}, N_{\beta}) = Z0$ 
return  $Z0, \text{table}$ 
end function

```

```

function SINGLEVESSELIMP( $ZL, s$ )
Output:  $Z0$ , Laplace transform of the impedance at  $x = 0$  given  $ZL$ , its value at  $x = L$ 

if  $s = 0$  then
     $Z0 = ZL + \frac{2(\gamma+2)\mu\lambda}{\pi r_0^3}$ 
else
     $\delta = 2\mu(\gamma + 2) / (\rho r_0^2)$ 
     $d_s = \sqrt{\pi r_0^2 / (C\rho s(s + \delta))}$  ▷ principal value
     $Z0 = \left( ZL + \frac{1}{s d_s C} \tanh \frac{L}{d_s} \right) / \left( s d_s C ZL \tanh \frac{L}{d_s} + 1 \right)$ 
end if
end function

```

condition can be used for such transient flows. We describe a general procedure for incorporating microvascular changes due to autoregulation into the structured tree.

In Sections 2.1 and 2.2, we recalled how to compute the impedance of a structured tree by analytically solving the linearized flow equations via Laplace transform. That construction assumes, within each vessel, all parameters to be constant. However, in the case of autoregulation, the unstressed vessel radius r_0 varies with time. Even though the tree hemodynamic equations are taken as linear in the state variables P and Q , the dependence on r_0 is nonlinear. We construct below an efficient and accurate parametrization of the effects of microvascular dilation/constriction on the impedance weights.

We begin by analyzing the effects of variations of the unstressed radii of the smaller arteries on the impedance of the structured tree. Assume that the unstressed radii of the smaller arteries (vessels with $r_0 < r_{AR} \triangleq 100\mu m$) are multiplied by a constant scaling factor C_{AR} . It is straightforward to compute, for various C_{AR} , the impedance weights $z_k(C_{AR})$ of the modified trees. We enforce

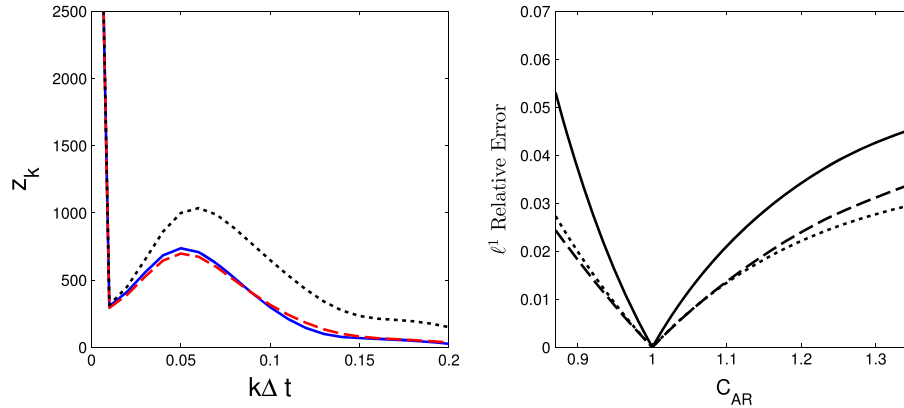


Figure 1. Left: impedance weights corresponding to the unmodified tree (black, dotted line), weights corresponding to tree with radii of smaller vessels multiplied by 1.35 (blue, solid line), and the unmodified weights multiplied by an exponential function according to (7) with $M_{AR} = -7.19$ (red, dashed line). Right: Error of similar fits for root radii of 0.1 (solid line), 0.2 (dashed line), and 0.33 (dotted line) for varying degrees of microvascular dilation/constriction.

the termination criterion $r_0 < r_{min}$ based on the *unmodified* radius, that is, the network structure remains unchanged for all values of C_{AR} . On the basis of extensive numerical experiments, we propose the following parametrization of the dependence of the z_k 's on C_{AR}

$$z_k(C_{AR}) \approx z_k(1)e^{M_{AR}k\Delta t}, \quad k = 0, \dots, N, \tag{7}$$

where $z_k(1)$ is the k -th weight of the unmodified tree, and Δt is the time step. For each value of C_{AR} , we determine a single value of M_{AR} that minimizes the relative error in the fit (7), that is,

$$E(r_{root}, C_{AR}) = \frac{\|\mathbf{z}(C_{AR}) - \mathbf{z}(1) \cdot * e^{M_{AR}[0, \dots, N]\Delta t}\|_1}{\|\mathbf{z}(C_{AR})\|_1}, \tag{8}$$

where $\mathbf{z} = [z_0, \dots, z_N]$, $\cdot *$ is the element-wise vector multiplication, and $\|\cdot\|_1$ is the ℓ_1 norm. Figure 1, left, displays this fitting procedure for a tree with root radius 0.2 cm and $C_{AR} = 1.35$. Approximation (7) is accurate over a wide range of root radii and dilation factors (C_{AR}), with the relative ℓ^1 error (8) never exceeding 6% for the cases considered (Figure 1, right).

We have verified the accuracy of this procedure for trees with root radii of 0.1, 0.2, and 0.33 cm (in all simulations performed in this work, root radii of outlet vessels range between 0.1 and 0.33 cm). For each value of C_{AR} , we compute the ‘‘resistance’’ at the root of the structured tree, $\hat{Z}_{root}(s = 0; C_{AR})$, which by definition corresponds to a ratio of time averaged pressure to time averaged flow. For each root radius value, we perform this fitting procedure for a range of C_{AR} corresponding to resistances between 74% and 130% of the unmodified tree resistance $\hat{Z}_{root}(s = 0; C_{AR} = 1)$. This roughly corresponds to typical lower and upper limits of the autoregulatory response [34, 36].

The aforementioned analysis provides a surrogate for the effects of different, time-invariant microvascular structures. It does not address the actual transient dynamics of the tree impedance in response to time-varying r_0 . However, the time scales of autoregulatory responses (generally 5–20 s, depending on the cardiovascular health of the individual [27, 37]) are substantially larger than the ‘memory’ of the structured tree. By memory, we mean the width of the support of the time-domain impedance (Figure 1, left), which is typically around 0.25 s and never more than 0.5 s in the cases considered in this paper. Thanks to these distinct time scales, it is thus reasonable to account for autoregulation-induced microvascular changes by

$$\tilde{z}_k(M_{AR}(t)) = z_k e^{M_{AR}(t)k\Delta t}, \quad k = 0, \dots, N. \tag{9}$$

The z_k 's in (9) are the weights for the unmodified tree and are computed prior to the simulation by the procedure described in Section 2.4. At each outlet, we simply impose condition (6) with the original impedance weights z_k replaced by the autoregulation-modified weights \tilde{z}_k from (9).

The dynamics of M_{AR} are governed by one's autoregulatory model of choice. We use here a simple ad hoc model to describe the variations of the tree resistance away from its baseline value of $R_{eq} = (P_{eq} - P_{term})/Q_{eq}$. If Q is the flow rate at the end of the outlet vessel, we consider the auxiliary equation

$$\frac{dx_{AR}}{dt} = G_{AR} \left(\frac{Q(t) - Q_{eq}}{Q_{eq}} \right), \quad (10)$$

where G_{AR} is the autoregulation gain. Equation (10) is similar to one component of the model used by Ursino *et al.* [38, 39]. Ursino *et al.* also incorporate an additional equation for CO₂ reactivity. While it would be straightforward to include this equation in our framework, (10) is adequate for the experiments of Section 3.3.

We obtain the auto-regulated value of the resistance R_{AR} from x_{AR} by imposing auto-regulatory limits. More precisely, baseline flow rate is generally only maintained for pressures between roughly 74% and 130% of baseline [34, 36]. We take this into account by passing x_{AR} into a sigmoidal function from [34, 35]

$$R_{AR} = \frac{R_{AR,L} + R_{AR,U} e^{x_{AR} - \hat{C}}}{1 + e^{x_{AR} - \hat{C}}} \quad (11)$$

where $\hat{C} = -\log[(R_{eq} - R_{AR,L}) / (R_{AR,U} - R_{eq})]$ with $R_{AR,L} = (0.74P_{eq} - P_{term})/Q_{eq}$ and $R_{AR,U} = (1.3P_{eq} - P_{term})/Q_{eq}$. The equilibrium pressures and flowrates for a particular outlet vessel, P_{eq} and Q_{eq} , are obtained by running a baseline simulation, as we do in Section 3.1. Finally, the impedance weights corresponding to a particular R_{AR} are found by solving

$$\sum_{k=0}^N \tilde{z}_k(M_{AR}) = R_{AR} \sum_{k=0}^N z_k, \quad (12)$$

for M_{AR} . In (12), \tilde{z}_k are the autoregulated impedance weights given by (9), and z_k are the unmodified weights computed prior to running the simulation.

When using implicit time-stepping, as in the present work, the aforementioned autoregulatory model can be implemented by merely adding two equations, (10) and (12), per outlet vessel to the nonlinear system that is solved at each time step. For our simulation of the systemic arterial tree, the system contains thousands of equations, most of which from the discretized macroscopic flow equations [(13) and (14)]; autoregulation adds thus minimal computation cost. With an explicit time stepping routine, one would need to solve (12) for M_{AR} at each time step after updating R_{AR} by (10) and (11). Because of the positivity of the weights z_k , there is, for each R_{AR} , a unique value of M_{AR} that solves (12). Furthermore, thanks to the relatively slow timescales of the autoregulation mechanisms, M_{AR} only changes by a small amount from one timestep to the next.

In summary, we incorporate autoregulation into the structured tree via a simple modification of the impedance weights through expression (9). This does not require the modification of the pre-simulation algorithm for computing the impedance weights discussed in Section 2.4. One may merely modify these weights on the fly through expression (9) during a simulation in accordance with an autoregulatory model of one's choosing, such as (10) and (11). The approach can, in principle, accommodate a broad class of autoregulation models such as those of Ursino [38, 39], the metabolic models of David *et al.* [34, 35] and the model of Spronck *et al.* [40].

3. RESULTS

To test the aforementioned condition, we apply it to the following standard one-dimensional model [10–15, 17, 41, 42] valid in the larger vessels of some commonly considered vascular networks:

Table II. Data for the network displayed in Figure 2.

Number	Name	r_t (cm)	r_b (cm)	L (cm)
1	Ascending aorta I	1.25	1.23	2.0
2,3	R, L coronary	0.30	0.30	10.0
4	Ascending aorta II	1.23	1.14	5.0
5	Anonyma	0.70	0.70	3.5
6, 19	R, L subclavian	0.44	0.43	3.4
7, 8	R, L brachial	0.43	0.28	40.6
9, 10	R, L ulnar	0.22	0.22	6.7
11, 12	R, L radial	0.17	0.14	23.5
13, 14	R, L vertebral	0.14	0.14	14.8
15	R common carotid	0.29	0.28	17.0
16	L common carotid	0.29	0.28	19.0
17	Aortic arch	1.14	1.11	1.8
18	Aortic arch	1.11	1.09	1.0
20	Thoracic aorta	1.09	0.85	18.8
21	Celiac axis	0.33	0.30	3.0
22	Abdominal aorta	0.85	0.83	2.0
23	Superior mesenteric	0.33	0.33	5.0
24	Abdominal aorta	0.83	0.80	2.0
25, 26	R, L renal	0.28	0.25	3.0
27	Abdominal aorta	0.80	0.79	1.0
28	Abdominal aorta	0.79	0.73	6.0
29	Inferior mesenteric	0.20	0.18	4.0
30	Abdominal aorta	0.73	0.70	3.0
31, 32	R, L external iliac	0.45	0.43	6.5
33, 34	R, L femoral	0.43	0.40	13.0
35, 36	R, L internal iliac	0.20	0.20	4.5
37, 38	R, L femoral	0.40	0.30	44.0
39, 40	R, L deep femoral	0.20	0.20	11.0
41, 42	R, L external carotid	0.15	0.15	17.7
43, 44	R, L internal carotid	0.20	0.20	17.7
45, 46	R, L middle cerebral artery	0.14	0.14	11.9
47, 48	R, L anterior cerebral artery A1	0.12	0.12	1.2
49, 50	R, L anterior cerebral artery A2	0.12	0.12	10.3
51	Anterior communicating artery	0.07	0.07	0.3
52, 53	R, L posterior communicating artery	0.07	0.07	1.5
54, 55	R, L posterior cerebral artery P2	0.10	0.10	8.6
56, 57	R, L posterior cerebral artery P1	0.11	0.11	0.5
58	Basilar	0.16	0.16	2.9

r_t denotes the vessel radius at the proximal end of the vessel, r_b is the radius at the distal end of the vessel, and L denotes the vessel length. Wherever possible, values were taken from Olufsen *et al.* [9]. Values for the ulnar/radial arteries were taken from Reymond *et al.* [43], and values for the Circle of Willis were taken from Sherwin *et al.* [44].

$$\partial_t A + \partial_x Q = 0, \tag{13}$$

$$\partial_t Q + \frac{\gamma + 2}{\gamma + 1} \partial_x \left(\frac{Q^2}{A} \right) + \frac{A}{\rho} \partial_x P = - \frac{2\pi\mu(\gamma + 2)}{\rho} \frac{Q}{A}. \tag{14}$$

We consider two cases: a simulation of the larger systemic arteries with periodized data from [9] (Section 3.1) and a non periodic Circle of Willis simulation in Section 3.2. We showed elsewhere [10, 17] that the general impedance condition discussed here yields results close to those corresponding to the periodic structured tree condition from [7–9] but has better stability. Comparisons with other types of boundary conditions can be found in [7, 8, 11, 17].

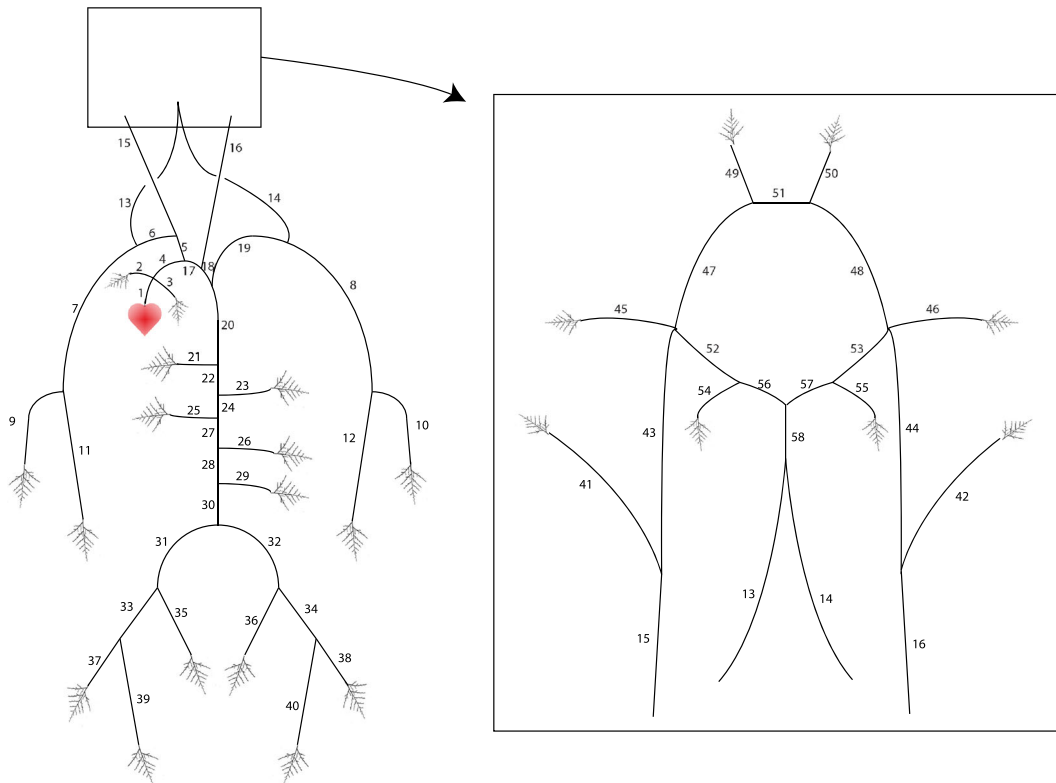


Figure 2. Network structure for the systemic arterial tree simulation; see Table II for detailed geometrical data.

3.1. Systemic arterial tree simulation

Consider the vascular network described in Figure 2. We compare our simulation results to flow rate data measured using magnetic resonance techniques in a 32-year old male weighing 65 kg and being 178 cm tall (see [9] for additional details regarding the data). The root vessel radii are taken from measurements while the length to radius ratio λ as used is a lone calibration parameter. To determine λ , we minimize the L_2 norms of the differences between the measured and simulated flowrates for the nine vessels for which measurements are available (Figure 3). We perform this optimization using MATLAB's trust region reflective algorithm and enforce symmetry in this calibration procedure. In other words, we require the length to radius ratio for corresponding right and left versions of the same vessel to be the same thereby reducing the number of calibration parameters by nearly half.

Computational results, displayed in Figure 3, show good agreement between the data and simulation[‡]. We do not have any measured pressure data, but at the aortic level, the pressure ranges between 70 and 125 mmHg (Figure 8), which is close to the typical physiological range.

[‡]We acknowledge that our fit is not quite as good as that of Olufsen *et al.* [9]. However, part of this is likely due to a small error in the network description in [9] that makes reproduction of their results impossible. Figure 1 and Table 1 of Olufsen *et al.* [9] indicate that, in their simulations, the subclavian arteries are terminal vessels (i.e., the radial and ulnar arteries are not included). Measured data at points E and J (Figure 2) would then appear to be measured at different points along the same uninterrupted vessel. However, the average flow rate over one period at point J is roughly 25% of that at point E. Flow conservation principles clearly imply that this is a contradiction. In [4], Azer and Peskin performed simulations on the network described in [9]. Azer and Peskin's simulations agreed reasonably well with the measured MRI data, except at point J where they differed from the data by roughly 400% (see [4], Figure 16, bottom left pane). The most likely explanation is that in the simulations of Olufsen *et al.*, the authors included a bifurcation at the distal end of the subclavian artery that was omitted from their Figure 1 and Table 1. Consultations with Olufsen have not managed to clarify this point. Making an educated guess as to the omitted vessels, we allow the subclavian arteries to bifurcate into the radial and ulnar arteries, and use data for the radii and lengths of these arteries from Reymond *et al.* [43]. Despite this uncertainty in the network structure, we obtain good agreement between our simulation results and measured data.

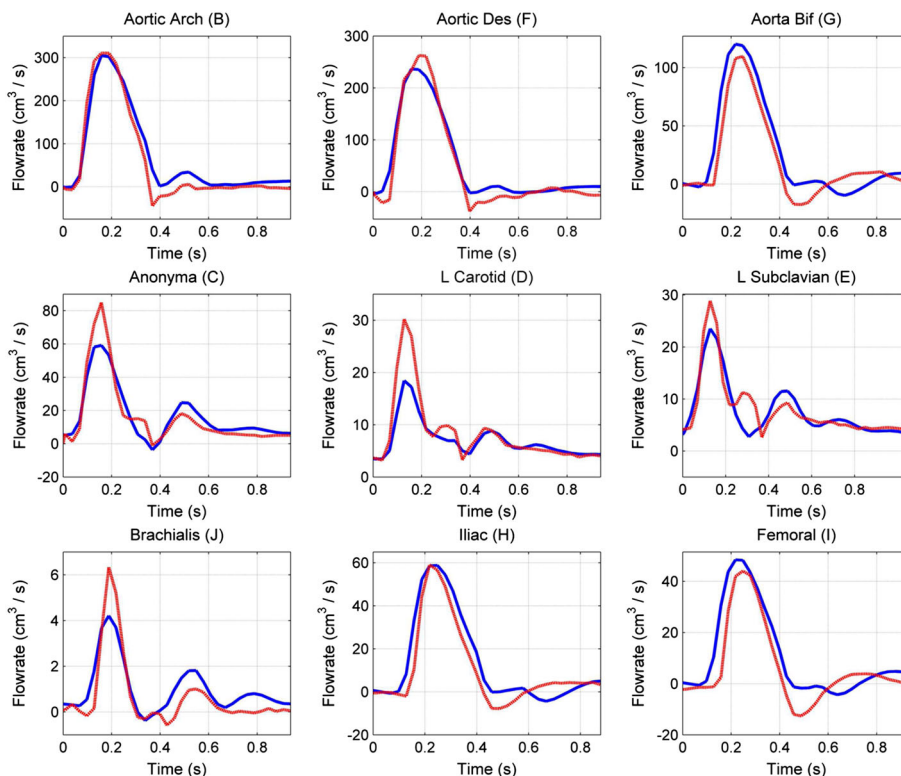


Figure 3. Comparison between simulated flows (blue) and measured data (red) for the systemic arterial tree. Time t is measured in seconds (s) and flow Q in cm^3/s . The locations at which measurements were taken are denoted on Figure 2.

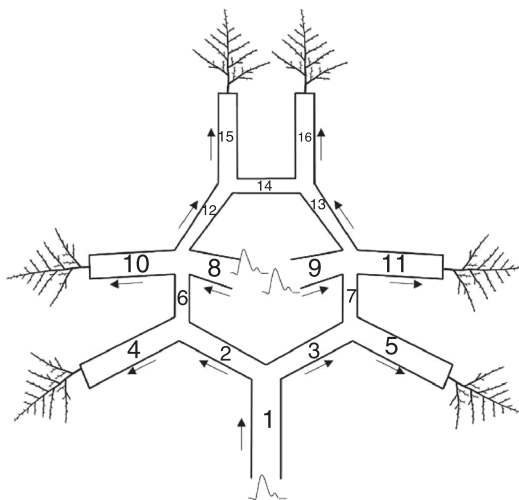


Figure 4. Schematic of the Circle of Willis; vessel name and size are given in Table III. Waveforms indicate inlets while trees signal outlets.

3.2. Circle of Willis simulation

The structure of the considered vascular network is displayed in Figure 4. Vessel radii and length measurements are given in Table III. Velocity data were obtained using digital transcranial Doppler technology[§] at locations approved by the Institutional Review Board at the Beth Israel Deaconess

[§]PMD 150, Terumo Cardiovascular Systems and Spencer Technologies Inc, Ann Arbor, MI and Seattle, VA USA.

Table III. Names and measured length/radii data (in cm) for the Circle of Willis (Figure 4).

	Name	r_0	L
1	BA	0.15	0.825
2	R. PCA 1	0.112	0.333
3	L. PCA 1	0.112	0.333
4	R. PCA 2	0.110	0.756
5	L. PCA 2	0.110	0.756
6	R. PCoA	0.0986	1.00
7	L. PCoA	0.0986	1.00
8	R. ICA	0.210	4.81
9	L. ICA	0.210	4.81
10	R. MCA	0.134	2.11
11	L. MCA	0.134	2.11
12	R. ACA 1	0.170	1.07
13	L. ACA 1	0.100	1.07
14	ACoA	0.100	0.20
15	R. ACA 2	0.115	2.30
16	L. ACA 2	0.115	2.30

Data are from [13]. BA, basilar artery; PCA, posterior cerebral artery; PCoA, posterior communicating artery; ICA, internal carotid artery; MCA, middle cerebral artery; ACA, anterior cerebral artery; ACoA, anterior communicating artery.

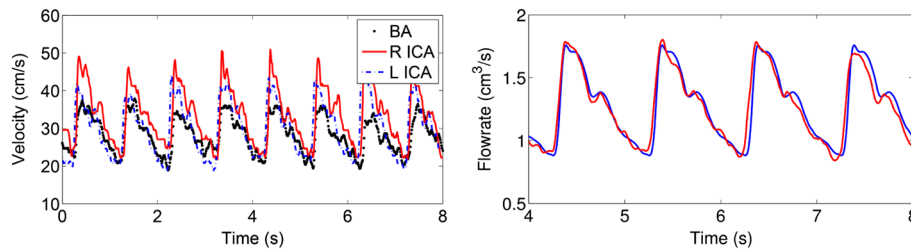


Figure 5. Left: measured velocities at the inlets. Right: representative difference between simulation results obtained with periodic inflows (blue) and raw inflows (red) in the anterior, middle, and posterior cerebral arteries (here, for the left posterior cerebral artery).

Medical Center. Specifically, our dataset includes velocity measurements at all inlets and outlets of the Circle of Willis (Figure 4). While transcranial Doppler has good time resolution (as opposed to MRI, for instance), the insonation angle, that is, the angle between the ultrasound probe and the vessel, is usually unknown. This clearly affects negatively to the accuracy of the measurements (see Bragg *et al.*, Cerebral blood flow measurements: intersubject variability using MRI and Transcranial Doppler, 2014, in preparation for more details).

Pressure was measured using a continuous noninvasive finger arterial blood pressure monitor in supine position[¶]. Vessel dimensions were measured from 3D MR angiography images (time of flight) using the Medical Image Processing, Analysis, and Visualization software from the Biomedical Research Services Station, NIH, Bethesda, MD; for each vessel, calculations were repeated at three locations and averaged. The accuracy is conservatively estimated at ± 0.4 mm, based on the image resolution. Measured velocities were imposed at the three inlets [basilar artery (BA) and left and right internal carotid arteries (ICAs)], see Figure 5, left, and the experiment is run to simulate 8 seconds in real time. The generalized impedance boundary condition was imposed at the six outlets [left and right anterior cerebral arteries (ACAs), MCAs and posterior cerebral arteries (PCAs)]. The simulation was calibrated by adjusting the values of λ to best match the velocity at the outlets.

[¶]Ohmeda, Monitoring Systems, Englewood.

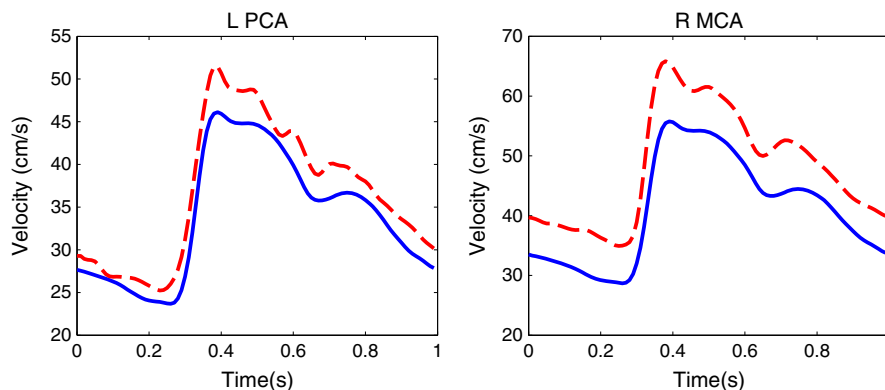


Figure 6. Comparison between simulated flows (blue) and measured data (red) for the Circle of Willis. Time t is measured in seconds (s) and velocity U in cm/s. See comment on data inconsistency in the text.

Representative results are displayed in Figure 6. The simulation results agree reasonably well with the data, and we now explain how the mild discrepancy in that figure stems either from errors in the measured velocity or geometric data for the Circle of Willis. Figure 6 clearly shows that our simulation results undershoot the measured velocities. We note however that the total measured flow into the Circle of Willis (contributions from the BA and ICAs) is 12.5% smaller than the combined measured outflow through the ACAs, MCAs and PCAs. Since the hemodynamic model conserves flow rate, we would expect that the simulated outflows would also be smaller than the measured outflows. This is precisely the case, with the simulated average outlet velocities being 12.1% less than the measured velocities. We hypothesize that, absent this systematic bias in the measured data, the agreement between model and data in Figure 6 would be improved even further.

Unlike the previous experiment (Section 3.1) where inflow data were imposed at only one location, the present simulation involves three inlets. Measurements at different locations are usually not taken simultaneously. Typically, in simulations like ours, the various inflow signals are put in phase before computation. To measure the effects of such phase shifts, we first run the previous experiment with in-phase and fully periodized inflows obtained from the measurements. The experiment is then repeated with the raw (non-periodic) data from Figure 5, left. The flowrates in the ACAs, MCAs, and PCAs are only minimally affected as shown by Figure 5, right.

While the overall flowrates in the communicating arteries are relatively small, they undergo dramatic changes when switching from periodized inflow conditions to the actual raw measurements (Figure 7).

In particular, the flowrates in both the right posterior communicating artery and the anterior communicating artery change by over 200%. The asymmetry of the results, visible from direct comparison of the left and right posterior communicating artery flows, results from the asymmetry of the ACAs for that specific patient (Table III). The high sensitivity to asymmetry and phase shifts of flowrates in the communicating arteries was also noted in [45]. Despite this high sensitivity of the flow rate time series values in these vessels, the time averaged flow rate at each point in the Circle of Willis remains nearly invariant, changing by no more than 5% between the periodized and raw data simulations. For example, despite the substantial variation between the two flowrates in the anterior communicating artery (Figure 7, bottom), the time averaged flowrates were nearly identical for the periodized data simulation ($-0.0251 \text{ cm}^3/\text{s}$) and raw data simulation ($-0.0262 \text{ cm}^3/\text{s}$).

3.3. Cerebral autoregulation simulations

We now incorporate the effects of cerebral autoregulation into the structured tree boundary condition using the procedure from Section 2.5. Specifically, we analyze autoregulatory responses to changes in mean aortic pressure (MAP) under three scenarios: a step-wise decrease in MAP [27, 37, 46], low frequency sinusoidal oscillations in MAP (which may be induced by deep breathing [47]), and

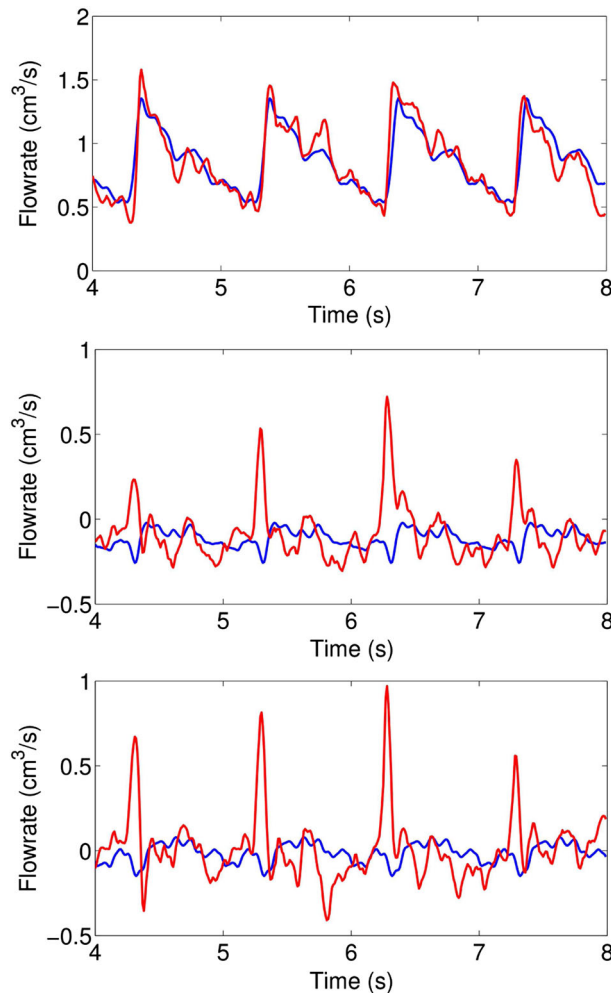


Figure 7. Difference between simulation results obtained using periodic inflows (blue) and raw inflows (red) in the left posterior communicating artery (top), right posterior communicating artery (middle), and anterior communicating artery (bottom).

a gradually increasing MAP [46]. For each of these three cases, we obtain results agreeing well with clinically measured data.

The above scenarios are considered in the general framework of the systemic arterial tree simulation of Section 3.1. We implement autoregulation at each of the six outlet vessels of the Circle of Willis (R/L MCA), R/L ACA, and R/L PCA, see vessels 45/46, 49/50 and 54/55 in Figure 2). While we only incorporate autoregulation in the cerebral vessels because this is where the measured data was collected, this procedure could easily be extended to other vessels. We determine the equilibrium pressure and flow values used in the autoregulation model equations (10, 12) by time averaging the values obtained by the baseline simulation from Section 3.1 at the distal end of each of the six respective outlet vessels of the Circle of Willis (these flow rate values are displayed in Figure 8, right). We set the autoregulation gain parameter $G_{AR} = 4$ in each cerebral outlet vessel. This value was obtained through trial and error so as to yield results in agreement with reported clinical measurements [27, 46] where flow returns to baseline within 5–7 s for individuals with healthy autoregulatory function (Figure 9). The return time to baseline can be considerably longer in individuals with impaired autoregulation [46]. We keep the value of G_{AR} unchanged for the final two simulations and also obtain results agreeing well with clinical measurements.

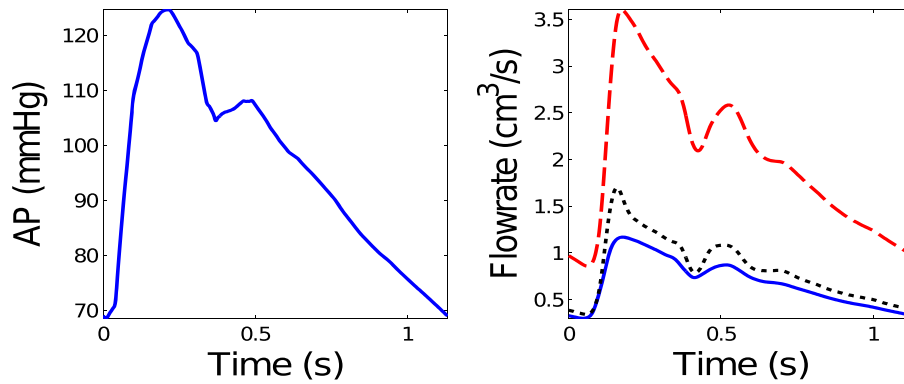


Figure 8. Baseline simulation results from Section 3.1. Left: pressure at the proximal end of the aorta. Right: flow rate at the distal end of the right posterior cerebral artery (blue, solid line), middle cerebral artery (red, dashed line), and anterior cerebral artery (black, dotted line). The periodic extension of the aortic pressure is modified according to the experiment at hand and then imposed as an inlet boundary condition. The cerebral flow rate information is averaged to compute Q_{eq} in (10) and (12).

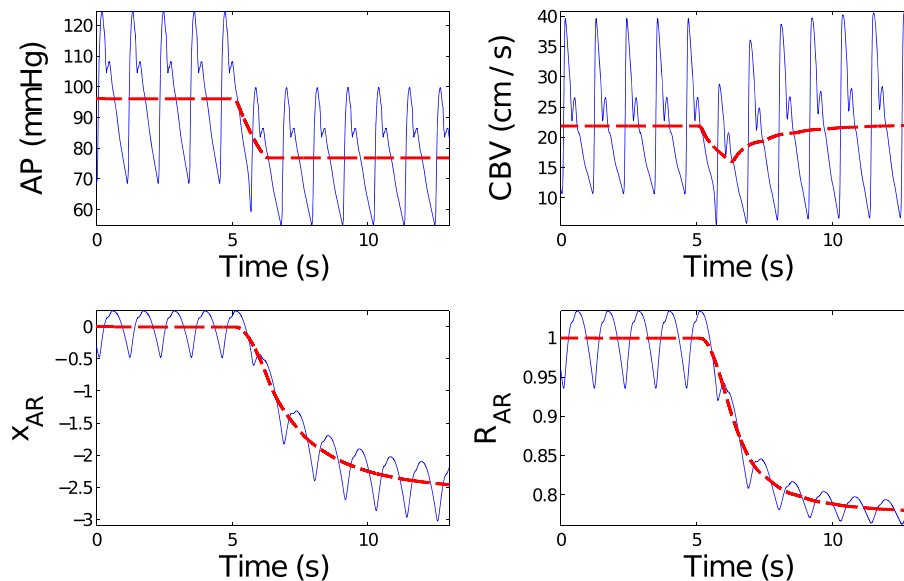


Figure 9. Aortic pressure (top left) and velocity (top right), x_{AR} (bottom left), and R_{AR} (bottom right) in the left posterior cerebral artery. The blue curves correspond to the exact values of each quantity, and the red curves are a moving average over one heartbeat.

In each of the three experiments in the succeeding text, we impose the following pressure inflow boundary condition at the proximal end of the aorta

$$P(t) = P_{baseline}(t)f(t),$$

where $P_{baseline}$ is the periodic baseline pressure at the aorta from the simulation performed in Section 3.1 (Figure 8, left). We modify this baseline pressure through the use of different functions $f(t)$ for each experiment. The corresponding simulations are identical aside from the choice of $f(t)$.

First, we simulate the effects of a sudden 20% drop in MAP. This is modeled through $f(t) = 0.9 + 0.1 \tanh(20(5T - t))$. The period of the baseline simulation is $T \approx 1.13$ s. The resulting aortic pressure is displayed in the top-left pane of Figure 9. This pressure drop induces a corresponding near-immediate flow decrease. After this initial decrease in flow, autoregulatory mechanisms reduce the cerebral tree resistance and the flow subsequently returns to baseline levels (Figure 9). This behavior has previously been observed experimentally [27, 37, 46] and numerically [34, 35].

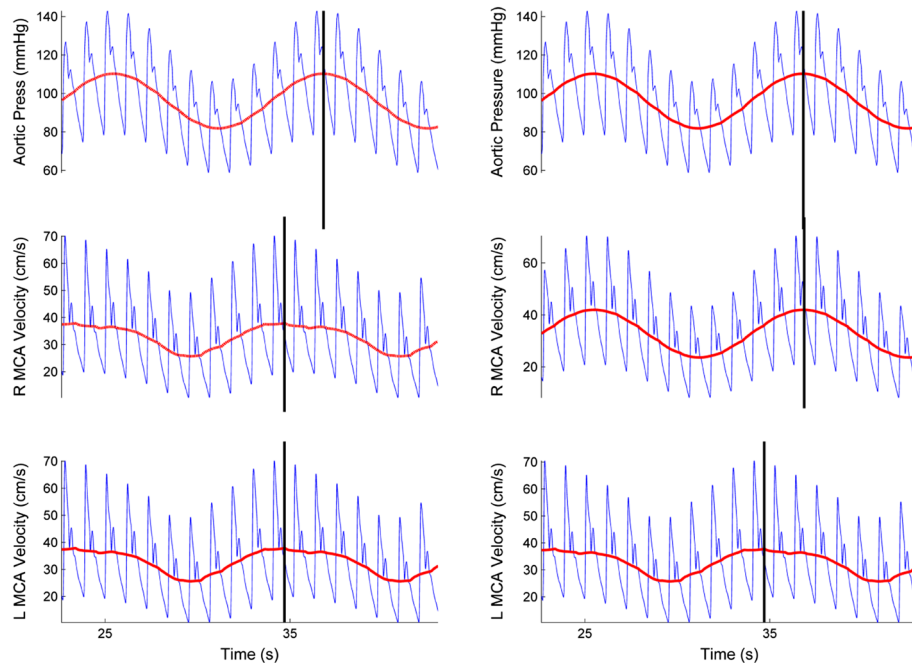


Figure 10. Left: aortic pressure and velocities in the R/L middle cerebral arteries with healthy cerebral autoregulation. Right: aortic pressure and middle cerebral artery (MCA) velocities with impaired autoregulation in the right MCA territory. The blue curves correspond to the exact values of each quantity, and the red curves are a moving average over one heartbeat.

In [47], Diehl *et al.* obtained clinical measurements of the effects of sinusoidal oscillations of MAP on cerebral blood velocity (CBV). These MAP oscillations had a period of roughly 10 s and were induced by instructing subjects to breathe in or to breathe out every 5 s. Diehl *et al.* found that this low frequency sinusoidal oscillation in MAP induced a similar oscillation in CBV. As a test of an individual's cerebral autoregulatory function, they measured the phase shift between the low frequency oscillations of MAP and CBV. Under the assumption that this phase shift would be 0° in the absence of autoregulation, the authors interpreted a larger phase shift angle as indicative of more optimal autoregulatory function. Their experiments supported this idea, as the average phase shift was 51.7° for patients with occlusive cerebrovascular disease, 26.8° for patients with arteriovenous malformations, and 70.5° for healthy patients.

Our model reproduces many of the clinical observations from [47] (Figure 10). The inlet boundary condition consists in setting the pressure at the aortic level to be equal to the baseline pressure from the simulation in Section 3.1 multiplied by $f(t) = 1 + 0.15 \sin(2\pi t/10T)$, where T is again the period of the baseline simulation. We take the value $G_{AR} = 4$ at each outlet to study the MAP/CBV relationship in the case of a patient with healthy autoregulatory function. To simulate the effects of impaired autoregulation due to a pathological condition, we set $G_{AR} = 0$ for the three outlet vessels on one side of the brain (R ACA, R MCA, and R PCA). For each case, the low frequency MAP oscillation induces a corresponding low frequency CBV oscillation. For the healthy case, we observe a phase difference of 76.5° , agreeing well with the measured value of 70.5° reported by Diehl *et al.* [47]. For the simulation with impaired autoregulation on one side of the brain, we see a phase difference of nearly zero (-1°) on the pathological side and a normal phase difference of 76° on the healthy side, which also agrees well with the clinically measured results of Diehl.

Finally, we simulate the experiments of Tiecks *et al.* [46], who studied the effects of continuous phenylephrine injection on CBV. This injection induced a gradual increase of MAP to roughly 20 mmHg above baseline. To simulate this, we set the aortic pressure to be equal to the baseline pressure multiplied by, for t between 10 and 60, $f(t) = 1 + 0.2(t - 10)/50$. We set $f(t) = 1$ for t less than 10, and $f(t) = 1.2$ for t bigger than 60 (Figure 11). In the absence of autoregulation, this pressure increase would induce a corresponding increase in CBV. However, Tiecks *et al.* found

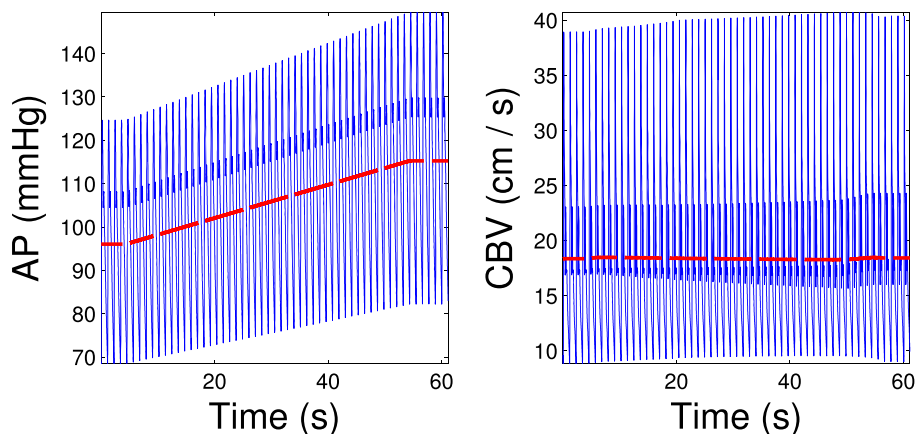


Figure 11. Left: Imposed pressure at the aorta. Right: velocity in the left anterior cerebral artery, which remains nearly unchanged despite upstream pressure variations due to autoregulation. Velocities in other cerebral arteries show similar behavior. The blue curves correspond to the exact values of each quantity, and the red curves are a moving average over one heartbeat.

that in the presence of an intact autoregulatory mechanism, CBV shows almost no change over the course of this pressure increase. Our simulations agree well with these clinically measured results—although there is some widening of the CBV pulse, the heartbeat-averaged CBV remains nearly constant in our simulations (Figure 11).

4. DISCUSSION

4.1. Computational cost

The computational cost of the impedance condition is proportional to the number of different vessels in the vascular tree. For a generic tree with ℓ generations, which number increases exponentially with ℓ while for the fractal trees considered in Section 2.2, it is only $\mathcal{O}(\ell^2)$. We precompute the impedance weights from (6) for each outflow vessel; this corresponds to $2N$ evaluations of the IMPEDANCE function per outflow vessel, where $N = \text{ceil}(1/\Delta t)$. Each evaluation of IMPEDANCE requires $\mathcal{O}(\ell^2)$ floating point operations. Typically, ℓ is no more than 30, resulting in a cost of a few thousand floating point operations per evaluation.

In short, the boundary condition represents a very small fraction of the overall cost of the computational simulations. However, the cost of the implementation described in Section 2 may be high if one requires tens of thousands of time steps per second, as may be the case if explicit time stepping is used. In this case, a simple way to extinguish the high computational cost would be to use a coarser time mesh for the convolution (6) than is used for the differential equation timestepping. This approach would require only mild modifications to the algorithm, and the fact that the impedance weights do not oscillate rapidly [10, 17] suggests that there would be little degradation to numerical accuracy. In our simulations, this procedure is not required because we use an implicit Euler timestepping routine with a time step of $\Delta t = 0.0025$ for the systemic arterial tree, and $\Delta t = 0.01$ for the Circle of Willis.

4.2. Autoregulation

We propose a physiologically based, yet computationally inexpensive, method for incorporating autoregulatory effects into vascular trees. In developing this method, we make a number of simplifying assumptions which represent possible sources of inaccuracy. First, only vessels whose radii fall under a strict threshold value are assumed to adaptively dilate/constrict. In addition, the radii are adapted through multiplication by a single, time varying factor. The effects of inhomogenous autoregulatory modification of the vascular tree merits further study. Such effects could likely be

Table IV. Tiered structure used in [17].

radius range	λ	ξ	ζ
$250\mu\text{m} < r$	10	2.50	0.4
$50\mu\text{m} \leq r \leq 250\mu\text{m}$	20	2.76	0.6
$r \leq 50\mu\text{m}$	30	2.90	0.9

The parameters ξ and ζ are defined by $r_p^\xi = r_{d1}^\xi + r_{d2}^\xi$ and $\zeta = \left(\frac{r_{d2}}{r_{d1}}\right)^2$.

incorporated into the structured tree in a straightforward manner. Some error is also introduced through our method of incorporating the effects of a changing microvasculature through a simple parametrization (9). However, we feel that the error introduced by this parameterization is small since, in spite of its simplicity, it leads to remarkably accurate results as displayed in Figure 1.

Despite the aforementioned limitations, our approach described in Section 2.5 provides a powerful new tool for incorporating autoregulation in hemodynamic simulations and does so through a combination of computational simplicity and physiological grounding. Furthermore, it is compatible with a wide class of existing autoregulation models.

4.3. Calibration

Most of the parameters defining the impedance condition can be measured and therefore the need for calibration is greatly reduced. The results from the previous section were obtained by calibrating the length to radius ratio λ individually for each tree. This follows the approach from [4, 18] and provides a mechanism to control the relative impedance between different outlets. For the systemic arterial tree simulation, we used values of λ between 10 and 60. For the Circle of Willis simulation, our calibration procedures yielded values of λ ranging from 13 to 19.

The aforementioned need for calibration is indicative of some shortcomings of the tree modeling. Indeed, there is ample physiological evidence that the scaling parameters defining a tree are not constant through it. While the use of a generic tree (with no fractal structure) is too computationally cumbersome, the tiered structure approach from [18] can be emulated and generalized.

For instance, the values given in Table IV are in agreement with most of the available data such as [48, 49] for the asymmetry of the vessels, [49–51] for the size of the vessels and [49, 52, 53] for the length to ratio parameter λ . We have successfully used these values in [17] in the case of the experiment from Section 3.1 with no calibration whatsoever. This very promising result does not directly generalize to organ specific simulation (such as the Circle of Willis simulation in Section 3.2), possibly because organ specific tree geometries should be developed.

In conclusion, the proposed method is efficient and reliable for general transient hemodynamics. It has the advantage of involving physiological parameters. Although, in this work, we required some calibration to match simulation results to measured data, we hypothesize that the need for calibration could be decreased further by the adoption of more realistic, organ-specific tree structures. These trees are constrained by the particular shape of the organ that they inhabit, and different organ shapes may induce different tree branching properties [54–57]. It may be possible to determine these organ specific tree properties by performing a constrained constructive optimization procedure to grow optimal trees within various organ geometries. Such a procedure has already been performed by Karch *et al* [58] to study the structure of the arterial tree between the epi- and endocardial layers of the human heart.

ACKNOWLEDGEMENTS

The authors are indebted to Vera Novak for the use of the cerebral blood flow data, as well as to Alison Marsden, Mette Olufsen, and Daniel Tartakovsky for helpful discussions. They also thank the referees for constructive and helpful remarks. Both authors acknowledge the support by the National Science Foundation (NSF) through grant DMS-0636590, and W.C. received support from NSF East Asia and Pacific Summer Institutes (EAPSI) award 1015642.

REFERENCES

1. Blanco P, Watanabe S, Feijóo R. Identification of vascular territory resistances in one-dimensional hemodynamics simulations. *Journal of Biomechanics* 2012; **45**:2066–2073.
2. Sherwin S, Formaggia L, Peiró J, Franke V. Computational modeling of 1D blood flow with variable mechanical properties and its application to simulation of wave propagation in the human arterial system. *International Journal for Numerical Methods in Fluids* 2003; **43**:673–700.
3. Vignon-Clementel I, Figueroa C, Jansen K, Taylor C. Outflow boundary conditions for three-dimensional finite element modeling of blood flow and pressure in arteries. *Computer Methods in Applied Mechanics and Engineering* 2006; **195**:29–32.
4. Azer K, Peskin C. A one-dimensional model of blood flow in arteries with friction and convection based on the Womersley velocity profile. *Cardiovascular Engineering* 2007; **7**:51–73.
5. Grinberg L, Karniadakis G. Outflow boundary conditions for arterial networks with multiple outlets. *Annals of Biomedical Engineering* 2008; **36**(9):1496–1514.
6. Lee J, Smith N. The multi-scale modelling of coronary blood flow. *Annals of Biomedical Engineering* 2012; **40**:2399–2413.
7. Olufsen M. Modeling the arterial system with reference to an anesthesia simulator. *Ph.D. Thesis*, Roskilde University, Denmark; 1998. 95–120.
8. Olufsen M. Structured tree outflow condition for blood flow in the larger systemic arteries. *American Journal of Physiology* 1999; **276**(Heart Circ. Physiol. 45):H257–H268.
9. Olufsen M, Peskin C, Kim W, Pederson E, Nadim A, Larsen J. Numerical simulation and experimental validation of blood flow in arteries with structured-tree outflow conditions. *Annals of Biomedical Engineering* 2000; **28**:1281–1299.
10. Cousins W, Gremaud P, Tartakovsky D. A new physiological boundary condition for hemodynamics. *SIAM Journal on Applied Mathematics* 2013; **73**:1203–1223.
11. Cousins W, Gremaud P. Boundary conditions for hemodynamics: The structured tree revisited. *Journal of Computational Physics* 2012; **231**:6086–6096.
12. Čanić S, Kim E. Mathematical analysis of the quasilinear effects in a hyperbolic model of blood flow through compliant axi-symmetric vessels. *Mathematical Methods in the Applied Sciences* 2003; **26**(14):1161–1186. DOI: 10.1002/mma.407.
13. DeVault K, Gremaud P, Novak V, Olufsen M, Vernieres G, Zhao P. Blood flow in the circle of Willis: modeling and calibration. *Multiscale Modeling and Simulation: a SIAM Interdisciplinary Journal* 2008; **27**:888–909.
14. Fernández M, Milišić V, Quarteroni A. Analysis of a geometrical multiscale blood flow model based on the coupling of ODEs and hyperbolic PDEs. *Multiscale Modeling and Simulation* 2005; **4**(1):215–236 (electronic). DOI: 10.1137/030602010.
15. Sherwin SJ, Franke V, Peiró J, Parker K. One-dimensional modelling of a vascular network in space-time variables. *Journal of Engineering Mathematics* 2003; **47**(3-4):217–250. DOI: 10.1023/B:ENGI.0000007979.32871.e2.
16. Steele B, Taylor C. Simulation of blood flow in the abdominal aorta at rest and during exercise using a 1-D finite element method with impedance boundary conditions derived from a fractal tree. *Proceedings of the 2003 ASME Summer Bioengineering Meeting*, Key Biscayne, FL, 2003.
17. Cousins W. Boundary conditions and uncertainty quantification for hemodynamics. *Ph.D. Thesis*, 2013.
18. Olufsen M, Steele M, Taylor C. Fractal network model for simulating abdominal and lower extremity blood flow during resting and exercise conditions. *Computer Methods in Biomechanics and Biomedical Engineering* 2007; **10**:39–51.
19. Torii R, Oshima M, Kobayashi T, Takagi K, Tezduyar TE. Coupling 3D fluid-structure interaction modeling of cerebral aneurysm with 0D arterial network model as boundary conditions. *Transaction of the Japan Society for Simulation Technology* 2009; **1**:81–90.
20. Lorthois S, Cassot F. Fractal analysis of vascular networks: insights from morphogenesis. *Journal of Theoretical Biology* 2010; **262**:614–533.
21. Caro C, Pedley T, Schroter R, Seed W. *The Mechanics of Circulation*. Cambridge University Press: Cambridge, UK, 2012.
22. Pries AR, Secomb TW, Gessner T, Sperandio MB, Gross JF, Gaehtgens P. Resistance to blood flow in microvessels in vivo. *Circulation Research* 1994; **75**:904–915.
23. Pries AR, Neuhaus D, Gaehtgens P. Blood viscosity in tube flow: dependence on diameter and hematocrit. *American Journal of Physiology* 1992; **263** (Heart Circ. Physiol. **32**):H1770–H1778.
24. Kano P, Brio M, Moloney J. Application of Weeks method for the numerical inversion of the Laplace transform to the matrix exponential. *Communications in Mathematical Sciences* 2005; **3**(3):335–372.
25. Lubich C. Convolution quadrature and discretized operational calculus. I. *Numerical Mathematics* 1988; **52**(2):129–145.
26. Lubich C. On the multistep time discretization of linear initial-boundary value problems and their boundary integral equations. *Numerical Mathematics* 1994; **67**(3):365–389.
27. Aaslid R, Lindegaard K, Sorteberg W, Nornes H. Cerebral autoregulation dynamics in humans. *Stroke* 1989; **20**(1):45–52.
28. Johnson PC. Autoregulation of blood flow. *Circulation research* 1986; **59**(5):483–495.

29. Paulson O, Strandgaard S, Edvinsson L. Cerebral autoregulation. *Cerebrovascular and Brain Metabolism Reviews* 1989; **2**(2):161–192.
30. Johnson PC. The myogenic response. In *Handbook of Physiology. The Cardiovascular System. Vascular Smooth Muscle*, Vol. II, Bohr DF, Somlyo AP, Sparks Jr. HV (eds). Am Physiol Soc: Bethesda, MD, 1980.
31. Rosengarten B, Huwendiek O, Kaps M. Neurovascular coupling and cerebral autoregulation can be described in terms of a control system. *Ultrasound in medicine & biology* 2001; **27**(2):189–193.
32. Kuschinsky W. Neuronal-vascular coupling. In *Optical Imaging of Brain Function and Metabolism 2*, Villringer A, Dirnagl U (eds). Springer: Berlin, Germany, 1997; 167–176.
33. Kavdia M, Popel A. Wall shear stress differentially affects NO level in arterioles for volume expanders and Hb-based O₂ carriers. *Microvascular Research* 2003; **66**(1):49–58.
34. Alastruey J, Moore S, Parker K, David T, Peiró J, Sherwin S. Reduced modelling of blood flow in the cerebral circulation: Coupling 1-D, 0-D and cerebral auto-regulation models. *International Journal for Numerical Methods in Fluids* 2008; **56**(8):1061–1067.
35. Moore S, David T. A model of autoregulated blood flow in the cerebral vasculature. *Proceedings of the Institution of Mechanical Engineers, Part H: Journal of Engineering in Medicine* 2008; **222**:513–530.
36. Strandgaard S. Autoregulation of cerebral blood flow in hypertensive patients. the modifying influence of prolonged antihypertensive treatment on the tolerance to acute, drug-induced hypotension. *Circulation* 1976; **53**(4):720–727.
37. Newell DW, Aaslid R, Lam A, Mayberg T, Winn H. Comparison of flow and velocity during dynamic autoregulation testing in humans. *Stroke* 1994; **25**:793–797t.
38. Ursino M, Ter Minassian A, Lodi CA, Beydon L. Cerebral hemodynamics during arterial and CO₂ pressure changes: in vivo prediction by a mathematical model. *American Journal of Physiology-Heart and Circulatory Physiology* 2000; **279**(5):H2439–H2455.
39. Ursino M, Giannessi M. A model of cerebrovascular reactivity including the Circle of Willis and cortical anastomoses. *Annals of biomedical engineering* 2010; **38**(3):955–974.
40. Spronck B, Martens E, Gommer E, van de Vosse FN. A lumped parameter model of cerebral blood flow control. *American Journal of Physiology-Heart and Circulatory Physiology* 2012; **303**:H1143–H1153.
41. Lee J, Smith N. Development and application of a one-dimensional blood flow model for microvascular networks. *Proceedings of the Institution of Mechanical Engineers, Part H: Journal of Engineering in Medicine* 2008; **222**:487–512.
42. Vignon I, Taylor C. Outflow boundary conditions for one-dimensional finite element modeling of blood flow and pressure wave in arteries. *Wave Motion* 2004; **39**:361–374.
43. Reymond P, Merenda F, Perren F, Rufenacht D, Stergiopoulos N. Validation of a one-dimensional model of the systemic arterial tree. *American Journal of Physiology-Heart and Circulatory Physiology* 2009; **297**:H208–H222.
44. Alastruey J, Parker K, Peiro J, Byrd S, Sherwin S. Modeling the circle of Willis to assess the effects of anatomical variations and occlusions on cerebral flows. *Journal of Biomechanics* 2007; **40**:1794–1805.
45. Castro M, Putman C, Cebal J. Patient-specific computational fluid dynamics modeling of anterior communicating artery aneurysms: a study of the sensitivity of intra-aneurysmal flow patterns to flow conditions in the carotid arteries. *American Journal of Neuroradiology* 2006; **27**:2061–2068.
46. Tiecks FP, Lam AM, Aaslid R, Newell DW. Comparison of static and dynamic cerebral autoregulation measurements. *Stroke* 1995; **25**:1014–1019.
47. Diehl RR, Linden D, Lucke D, Berlit P. Phase relationship between cerebral blood flow velocity and blood pressure. *Stroke* 1995; **26**:1801–1804.
48. Kalsho G, Kassab G. Bifurcation asymmetry of the porcine coronary vasculature and its implications on coronary flow heterogeneity. *American Journal of Physiology-Heart and Circulatory Physiology* 2004; **287**:H2493–H2500.
49. van Bavel E, Spaan J. Branching patterns in the porcine coronary arterial tree: estimation of flow heterogeneity. *Circulation Research* 1992; **71**:1200–1212.
50. Huo Y, Kassab G. Intraspecific scaling laws of vascular trees. *Journal of the Royal Society Interface* 2012; **9**:190–200.
51. Rossitti S, Lofgren J. Vascular dimensions of the cerebral arteries follow the principle of minimum work. *Stroke* 1992; **34**:371–377.
52. Nordsletten D, Blackett S, Bentley M, Ritman E, Smith N. Structural morphology of renal vasculature. *American Journal of Physiology-Heart and Circulatory Physiology* 2006; **291**:H296–H309.
53. Zamir M. On fractal properties of arterial trees. *Journal of Theoretical Biology* 1999; **197**:517–526.
54. Bui A, Manasseh R, Liffman K, Sutalo I. Development of optimized vascular fractal tree models using level set distance function. *Medical Engineering & Physics* 2010; **32**:790–794.
55. Blanco P, de Queiroz R, Feijóo R. A computational approach to generate concurrent arterial networks in vascular territories. *International Journal for Numerical Methods in Biomedical Engineering* 2013; **29**:601–614.
56. Hirsch S, Reichold J, Schneider M, Szekely G., Weber B. Topology and hemodynamics of the cortical cerebrovascular system. *Journal Of Cerebral Blood Flow and Metabolism* 2012; **32**:952–967.
57. Reichold J, Stampanoni M, Keller A, Buck A, Jenny P, Weber B. Vascular graph model to simulate the cerebral blood flow in realistic vascular networks. *Journal Of Cerebral Blood Flow and Metabolism* 2009; **29**:1429–1443.
58. Karch R, Neumann F, Neumann M, Schreiner W. Staged growth of optimized arterial model trees. *Annals of Biomedical Engineering* 2000; **28**:495–511.